JOURNAL OF MATERIALS SCIENCE **37** (2002) 3023–3034

Ductile layer toughening of brittle intermetallic composites

J. LOU
The Princeton Materials Institute and The Department of Mechanical and Aerospace Engineering, Princeton University, Olden Street, Princeton, NJ 08544, USA

F. YE
Corning Lasertron, Inc., Bedford, MA 01730, USA

M. Li
Spectra-Physics Lasers, Inc., Mountain View, CA 94043, USA

W. O. SOBOYEJO
The Princeton Materials Institute and The Department of Mechanical and Aerospace Engineering, Princeton University, Olden Street, Princeton, NJ 08544, USA
E-mail: soboyejo@princeton.edu

This paper presents the results of a combined experimental and theoretical study of the ductile layer toughening of brittle intermetallics. Following a brief description of small- and large-scale bridging models for the estimation of the crack-tip shielding due to small- and large-scale bridging, the effects of ductile layer toughening are examined in a gamma-based titanium aluminide alloy (Ti-48Al) reinforced with TiNb strips; $MoSi_2$ reinforced with Nb layers, and NiAl reinforced with V layers with different thicknesses. In all cases, the measured resistance-curves are well predicted by existing small- and large-scale bridging models. The intrinsic specimen-independent toughness values are also shown to increase with increasing layer thickness, in the case of the NiAl/V composites. Finally, the general implications of the results are discussed for the toughening of brittle matrix composites under monotonic and cyclic loading.

1. Introduction

Since the original discovery of ductile phase toughening by Krstic [1, 2], significant efforts have been made to explore the potential use of ductile layer reinforcements in the toughening of brittle matrices [3–15]. Some of the early work was done by Ashby and co-workers [15], who explored the potential for ductile phase toughening using a model lead/glass system. Following the early work of Ashby *et al.* [15], Budiansky, Amazigo and Evans (BAE) [16] presented a theoretical framework for the estimation of crack-tip shielding due to small-scale bridging. Subsequent work by Bloyer *et al.* [4, 5], Odette *et al.* [10], Zok and Hom [17], and Li and Soboyejo [18] later extended the modeling framework to the prediction of crack-tip shielding due to large-scale bridging.

Much of the early work focused on the toughening of brittle ceramics [1, 2, 15, 16]. For example, the early work of BAE [16] relied on the use of metal-reinforced ceramics in the validation of their small-scale bridging models. Similarly, Ashby and co-workers [15] focused on the lead/glass system, while Krstic [1, 2] worked on the WC/Co system that is now used in cutting tool applications. Most of the early works explored the use of ductile particles or fibers in the toughening of brittle ceramics [19–22] or intermetallics [23–25]. However, it was later recognized that ductile layer toughened ceramics [26, 27] and intermetallics [4–6, 12, 18, 28] offer even greater potential for the engineering of ductile phase toughened composites.

Prior efforts to explain the measured resistance-curves in ductile layer composites were limited largely by the complicated iterative schemes in the rigorous fracture mechanics approaches that were used to estimate the shielding due to large-scale bridging [10, 17]. These iterative schemes [10, 17], which often have convergence problems, limited the extent to which they can be used to provide routine estimates of the resistance-curve behavior. However, most recently, Bloyer *et al.* [4–6] and Li and Soboyejo [18] have shown that simple estimates of resistance-curve behavior can be obtained using weighted layer traction functions developed by Fett and Munz [29].

The current paper presents a combined experimental and theoretical framework that can be used to assess the overall toughening potential of ductile layer-reinforced composites. The weighted layer tractions of Fett and Munz [29] are used to assess the shielding effects of large-scale bridging. A small-scale bridging expression from the handbook of Tada *et al.* [30] is also to estimate the overall toughening levels during the initial stages of resistance-curve behavior. The small- and large-scale bridging models are shown to provide good estimates of the measured resistance-curve behavior in: a gamma titanium aluminide intermetallic (Ti-48Al) reinforced with TiNb strips; $MoSi_2$ reinforced with Nb layers, and NiAl reinforced with V layers. The implications of the results are then discussed for the design of ductile phase toughened composites with brittle matrices.

2. Micromechanical modeling

The problem of small-scale bridging (small bridging zone compared to crack size) was modeled analytically by Budiansky *et al.* [16]. Assuming either rigid/perfectly plastic, or elastic perfectly plastic behavior, they obtained a number of solutions for the estimation of toughness due to crack bridging by ductile particles. Most of the expressions in [16] do not include a bridging length scale. However, one of the equations, which was obtained essentially from Tada *et al.* [30], did include a bridging length scale. This gives the toughening ratio due to crack bridging, λ_b, to be:

$$\lambda_b = \frac{K}{K_m} = 1 + \sqrt{\frac{2}{\pi}}\frac{f}{K_m}\int_0^L \frac{\alpha\sigma(x)}{\sqrt{x}}\,dx \qquad (1)$$

where α is a constraint/triaxiality factor, $\sigma(x)$ represents the bridging traction across the ductile reinforcements, x is the distance from the crack face behind the crack-tip, and L is bridging length, which is equal to the distance from the crack-tip to the last unfractured reinforcement.

The above analysis applies largely to the problem of small-scale bridging, which is generally encountered in particulate-reinforced composites [3, 16, 22]. However, in the case of ductile fiber-reinforced and ductile layer-reinforced composites, the lengths of bridging zones are generally observed to be comparable to the overall crack dimensions [4–6, 14]. Under such conditions, large-scale bridging models [4–6, 10, 30–32] are needed to estimate the shielding contributions from crack bridging. The early large-scale bridging models were first formulated by Odette *et al.* [10] and Zok and Hom [17]. Subsequent work by Cox and co-workers [33, 34] also established self-consistent methods for the analysis of large-scale crack bridging. However, these large-scale bridging models often require iterative methods/algorithms that may have convergence problems associated with them.

A simpler large-scale bridging model was, therefore, employed in the current study. This model, which was first proposed by Bloyer *et al.* [5, 6], utilizes weight functions by Fett and Munz [29], in the estimation of the weighted distributions of bridging traction across the individual reinforcements (Fig. 1). The shielding due to large-scale bridging, ΔK_{lsb}, may thus be expressed as:

$$\Delta K_{lsb} = \int_L \alpha\sigma(x)h(a,x)\,dx \qquad (2)$$

where L is the length of the bridge zone, α is a constraint/triaxiality factor, $\sigma(x)$ is a traction function along the bridge zone, and $h(a,x)$ is a weight function given by Fett and Munz [29]:

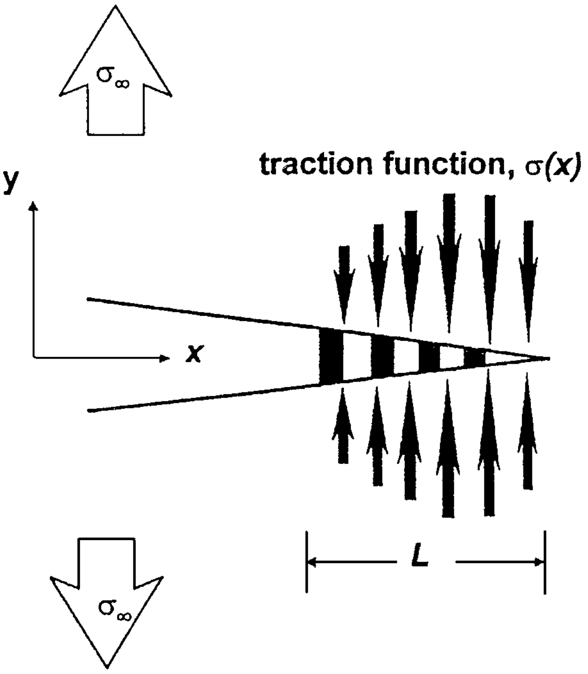

Figure 1 Schematic representation of a large-scale bridging model (After Bloyer *et al.* [5]).

$$h(a,x) = \sqrt{\frac{2}{\pi a}}\frac{1}{\sqrt{1-\frac{x}{a}}} \times \left[1 + \sum_{(\nu,\mu)} \frac{A_{\nu\mu}\left(\frac{a}{W}\right)}{\left(1-\frac{a}{W}\right)}\left(1-\frac{x}{a}\right)^{\nu+1}\right] \qquad (3)$$

where a is the crack length and W is the specimen width. The resistance-curve behavior may now be estimated by a simple application of the principle of linear superposition.

This gives the following expression for the estimation of the stress intensity factors along the resistance-curve:

$$K = K_i + \Delta K_{lsb} \qquad (4)$$

where K_i is the initiation toughness required for renucleation ahead of the first ductile layer encountered by the propagating crack, and ΔK_{lsb} is given by Equation 2 for large-scale bridging.

3. Materials and microstructures

The Ti-48Al + 20 vol% TiNb composite was produced by phase blending of Ti-48Al and TiNb powders. The Ti-48Al was produced by Nuclear Metals, Inc., Concord, MA, using the plasma rotating electrode process, and the TiNb was produced by Pratt and Whitney, West Palm Beach, FL, using a gas atomization process. The phase blended powders were canned in Ti-6Al-4V and extruded at 1343°C at the Wright-Patterson Air Force Base, Dayton, OH, with a reduction ratio of 14:1. Monolithic Ti-48Al was also extruded under the same conditions. The resulting microstructures obtained for

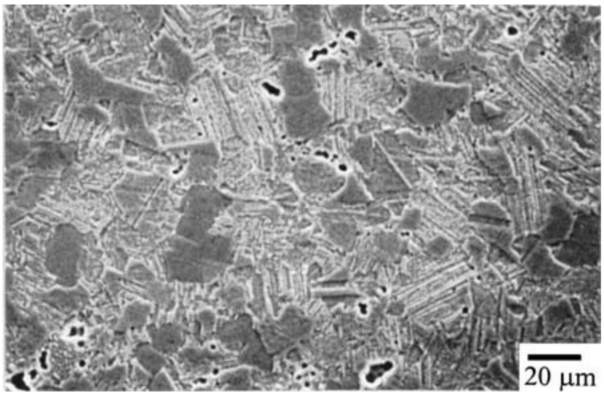

Figure 2 Optical micrograph of the monolithic gamma-(Ti-48Al) alloy.

the monolithic and composite gamma-based alloys are shown in Figs 2 and 3. The Ti-48Al alloy had a duplex as-extruded microstructure consisting of 18 μm lamellar $\alpha_2 + \gamma$ packets/colonies and 16 μm equiaxed γ grains. The typical γ lath widths were $\sim$0.26 μm, and the lath spacings were $\sim$0.65 μm in the as-extruded condition (Fig. 2). The Ti-48Al + 20 vol% TiNb composite structure consisted of elongated ($\sim$1000 μm) strips of TiNb (Fig. 3a and b), a predominantly γ interface between the reinforcements and the matrix (Fig. 3c), and a matrix with a duplex microstructure with equiaxed γ grains and wavy $\alpha_2 + \gamma$ lamellae (Fig. 3c). Note that the Nb reinforcement is labeled "c" in Fig. 3c. Material properties of TiAl/TiNb composite are summarized in Table I.

TABLE I Material properties of TiAl/TiNb composite

Material	Yield stress (MPa)	Ultimate tensile stress (MPa)	Plastic elongation to failure (%)
Ti-48Al	594	686	1.7
Ti-48Al + 20 vol% TiNb	–	523	–

The −325 mesh (25–30 μm average size) NiAl powders that were used in this study were procured from Homogeneous Metals, Inc., Clayville, NY. The vanadium strips with thickness of 100, 200 and 400 μm were supplied by Fine Metals Corp., Ashland, VA. Model NiAl composites reinforced with 20 vol% of V were produced by manual lay-up of NiAl powders on the layered reinforcements inside stainless steel cans. After manual lay-up, the cans were evacuated and sealed by electron beam welding. The evacuated cans were then hot isostatic pressed under 207 MPa pressure at 1100°C for 4 hours. Typical microstructures of the NiAl/V microlaminates are presented in Fig. 4. These show relatively uniform distributions of vanadium layers in a matrix of NiAl. The average size of NiAl grains measured by image analysis was about 25 μm. A small interfacial layer was also observed to form between the NiAl and vanadium layers (Fig. 4d). Semi-quantitative energy dispersive X-ray (EDX) spectroscopy revealed that this layer consisted of $\sim$11.8 at.% Ni, $\sim$11.6 at.% Al and $\sim$76.6 at.% V. The interfacial layers were approximately 5–10 μm thick in all the composites that were

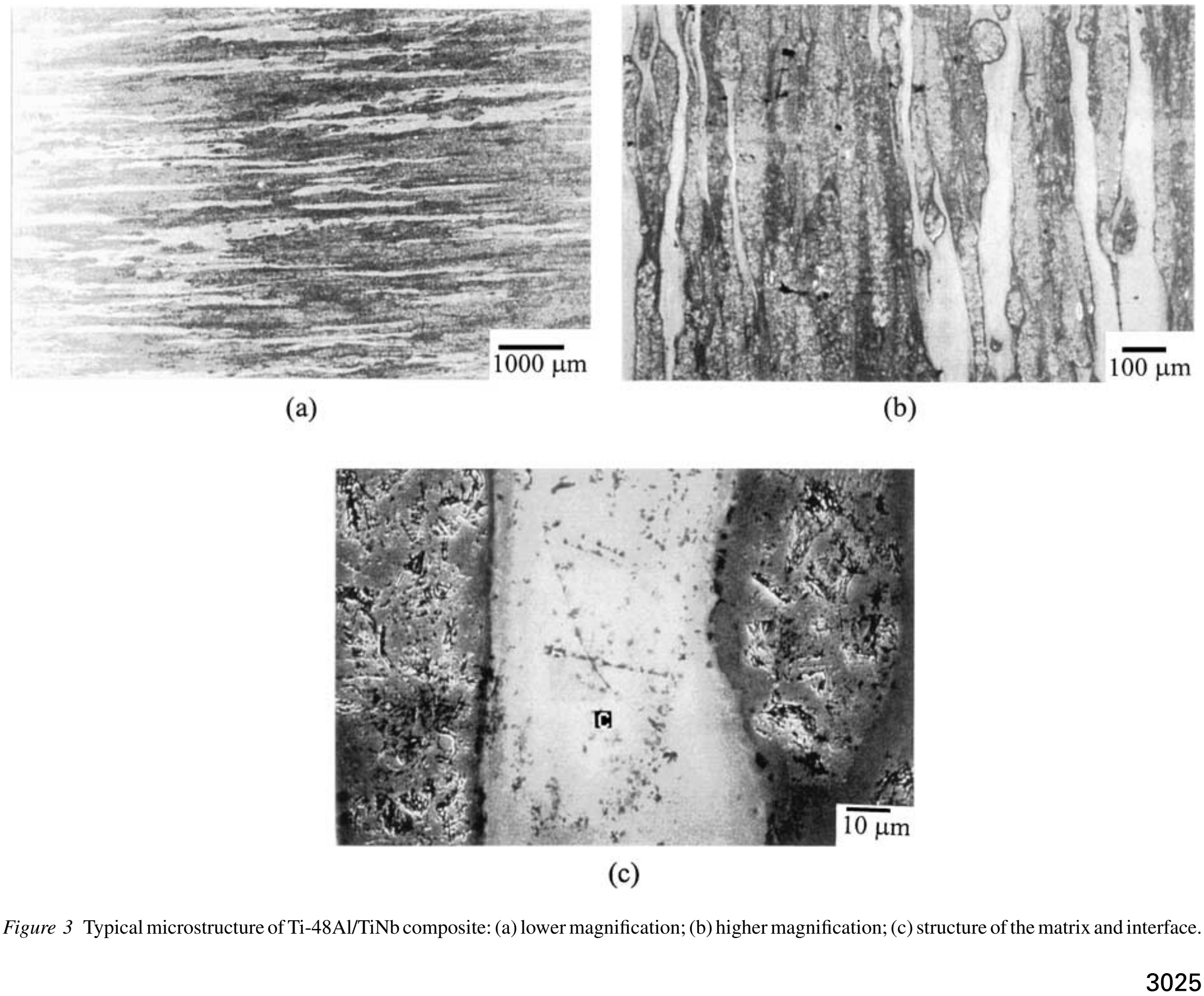

(a)

(b)

(c)

Figure 3 Typical microstructure of Ti-48Al/TiNb composite: (a) lower magnification; (b) higher magnification; (c) structure of the matrix and interface.

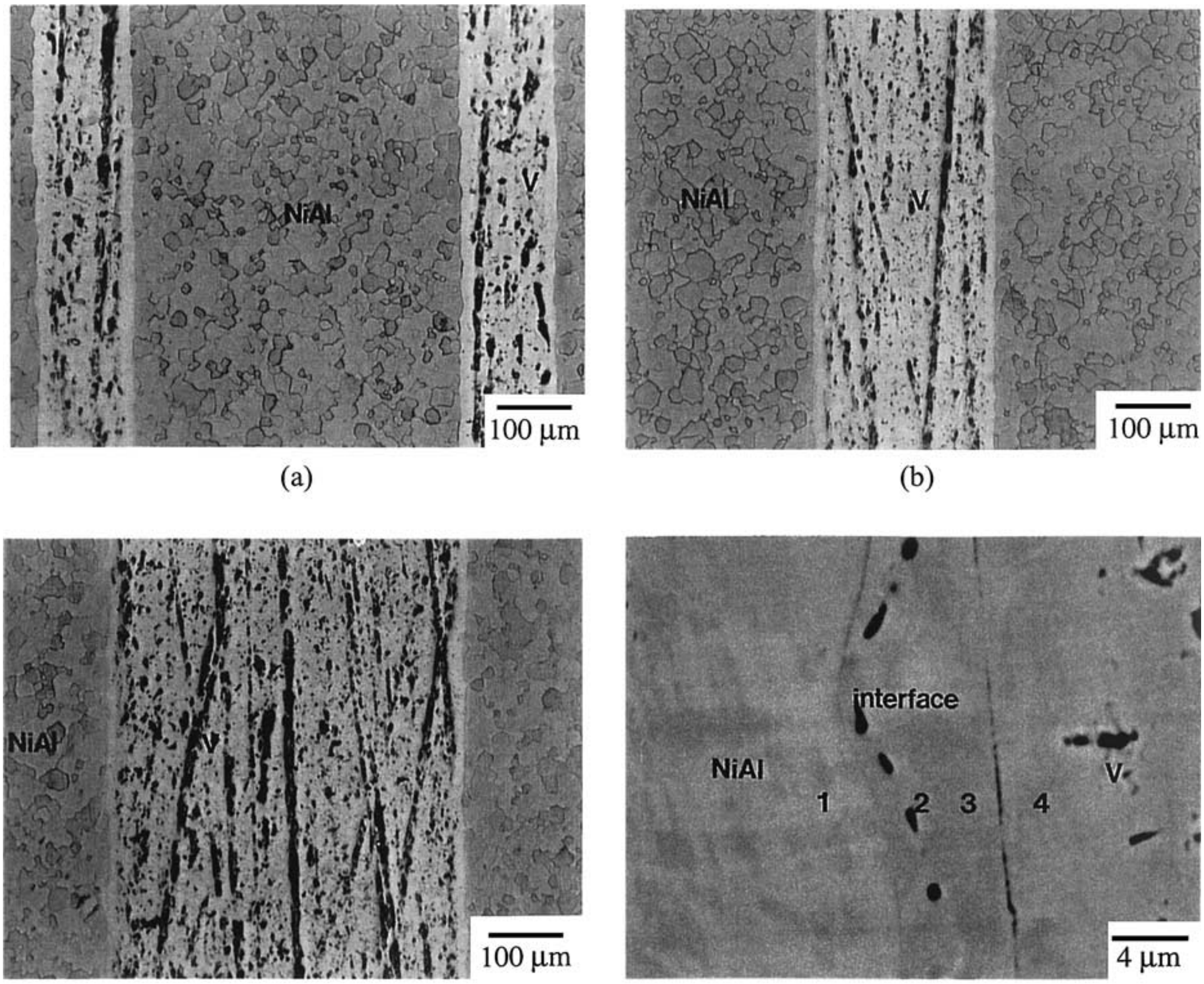

Figure 4 Typical microstructure of NiAl/V composites: optical micrograph of NiAl composites reinforced with (a) 100 m thick V layer, (b) 200 m thick V layer, (c) 400 m thick V layer, and (d) SEM micrograph of interface between NiAl and V layers.

TABLE II Material properties of the constituent component of NiAl/V composite

Material	Yield stress (MPa)	Young's modulus (GPa)	Poisson's ratio (ν)
NiAl	–	188	0.31
V	447	103	0.36

TABLE III Material properties of the constituent component of $MoSi_2$/Nb composite

Material	Yield stress (MPa)	Young's modulus (GPa)	Poisson's ratio (ν)
$MoSi_2$	–	380	0.17
Nb	245	103	0.36

produced. Material properties of the constituent component of NiAl/V composite are summarized in Table II.

The −325 mesh (approx. 44 μm average diameter) $MoSi_2$ powder used in this study was purchased from Cerac, Milwaukee, MI. The 200 μm Nb layer were purchased from Nuclear Metals, Henderson, NV. The laminate-reinforced composites were produced by manual lay-up of 200 μm diameter laminates on a Nb wire frame, evacuated (10^{-4} Pa) and sealed by electron beam welding. The canned material was then hot isostatic pressed (HIPing) under 207 MPa pressure, at 1400°C for 4 hours. The resulting compact was cooled slowly (over a period of 10 hours) to room temperature to minimize thermal gradients and cracking. The resulting microstructures of Nb laminate-reinforced composites are presented in Fig. 5 Interfacial phases of $MoSi_2$/Nb composites under similar processing condition have been determined by Lu *et al.* [35] to be Mo_5Si_3 and $(Mo, Nb)_5Si_3$ using electron diffraction and energy dispersive X-ray (EDS) spectroscopy technique. Similar interfacial layers were observed between the Nb and $MoSi_2$ layers in this study using EDS analysis. Material properties of the constituent component of $MoSi_2$/Nb composite are summarized in Table III.

4. Experimental procedures

In an effort to establish a general framework for the modeling of ductile layer toughening of intermetallic materials, fracture/resistance curve experiments were performed on the three systems described in the previous section. Hence, the systems that were tested include: Ti-48Al reinforced with 20 vol% of TiNb strips; $MoSi_2$ reinforced with Nb layers, and NiAl reinforced

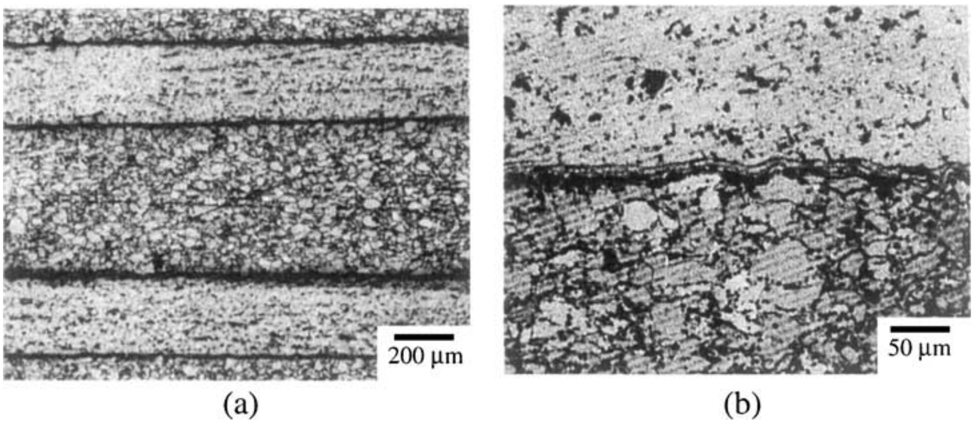

Figure 5 Typical microstructures of $MoSi_2$/Nb composites: (a) laminate distribution; (b) laminate/matrix interface.

with 20 vol% V layers with three different layer thicknesses (100, 200 and 400 μm).

The resistance-curve experiments were performed on 50 mm long single edge notched bend (SENB) specimens with rectangular cross-sections (6 mm × 12 mm). The specimens, which were produced via electron-discharge machining (EDM), had initial notch-to-width ratios, a/W, of ~0.40. After diamond polishing of the sides of the SENB specimens, and precracking under far-field compression [36], resistance-curve experiments were performed under three-point bend loading. The SENB specimens were tested under load-control in a servo-hydraulic testing machine.

Initial loads corresponding to stress intensity factors below the matrix toughness values reported for Ti-48Al (15 MPa$\sqrt{}$m) [22], $MoSi_2$ (3.6–4.0 MPa$\sqrt{}$m) [22] and NiAl (4–6 MPa$\sqrt{}$m) [18] were applied. The loads were increased in incremental steps between ~0.025 and 0.05 of the prior maximum loads. Following each load increment, the amount of stable crack growth was studied with an optical microscope. The crack/microstructure interactions were also elucidated via ex-situ optical and scanning electron microscopy. The experiments were continued until final fracture occurred. The fracture modes were then studied using scanning electron microscopy.

5. Results and discussions

5.1. Ti-48Al + 20 vol% TiNb

Stable crack initiation occurred in this composite at the matrix toughness of ~15 MPa$\sqrt{}$m [22] (Fig. 6). The initial resistance curve was very steep during the early stages of crack growth. However, a gradual transition to near-steady-state condition was observed during the final stages of crack growth (Fig. 6). The measured resistance-curve behavior was associated with the interactions of the crack with TiNb strips that bridged the crack faces (Fig. 7). This suggested that the measured resistance-curve behavior was due largely to the shielding effects of crack bridging.

Since the amount of stable crack growth ($\Delta a \leq$ 0.55 mm) was relatively small, only the small-scale bridging model (Equation 1), was applied to the prediction of resistance-curve behavior. The predicted resistance-curve is shown by the solid line in Fig. 6. This

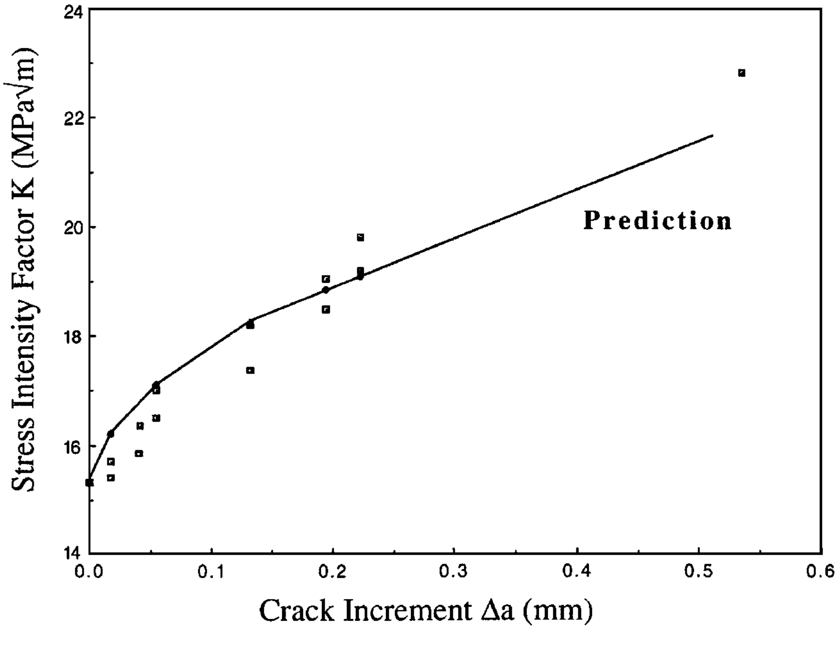

Figure 6 Comparison of measured and predicted resistance-curves obtained for TiAl/TiNb composites using small-scale bridging model.

Figure 7 Crack/microstructure interactions in TiAl/TiNb composites.

TABLE IV Parameters used in the prediction for TiAl/TiNb composite

Type of reinforcement	V_f	L (mm)	α	λ_b	ΔK_b (MPa$\sqrt{}$m)
20 vol% TiNb	0.2	1	1	1.3	5.1

was obtained using parameters summarized in Tables I and IV. Note that the predictions are in close agreement with the measured resistance-curve. Furthermore, no fitting functions are required to capture the curvature and magnitudes of the measured resistance-curves.

5.2. MoSi$_2$/Nb microlaminates

The resistance-curve obtained from the MoSi$_2$/Nb microlaminate is presented in Fig. 8. As in the case of the Ti-48Al/TiNb composite, the MoSi$_2$/Nb exhibits strong initial resistance-curve behavior, with a gradual transition to a steady-state. As in the case of the Nb fiber-reinforced MoSi$_2$ composites discussed in detail in [37], the measured resistance-curves in the MoSi$_2$/Nb microlaminates were due to the development of a large-scale bridging zone (Fig. 9). The cracks initiated in the MoSi$_2$ matrix, and extended rapidly to the Nb layers, where they were retarded. Renucleation then occurred on the other sides of the Nb layers, as the loads were increased in incremental stages to leave behind a large-scale bridging zone with plastically deformed Nb layers (Fig. 9).

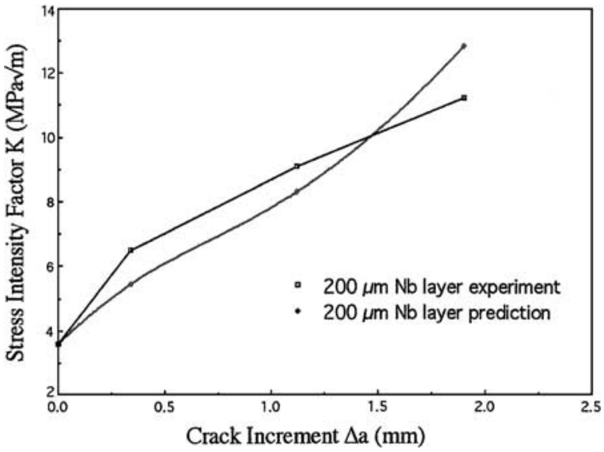

Figure 8 Comparison of measured and predicted resistance-curves obtained for MoSi$_2$/Nb composites.

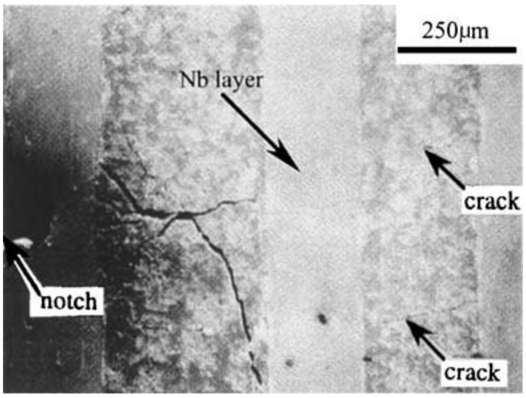

Figure 9 Crack/microstructure interactions in MoSi$_2$/Nb composites.

The predicted resistance-curves obtained from small-scale ($\Delta a \leq 0.5$ mm) and large-scale ($\Delta a \geq 0.5$ mm) bridging models are presented in Fig. 8. These were obtained using Equations 1–4 and parameters summarized in Tables II and V. The agreement between the predicted and measured resistance-curves is generally very good. However, the curvature of the large-scale bridging predictions is opposite to that of the measured resistance-curves. This is a common feature of such models [4–6, 10, 17, 18].

It is also important to note here that large-scale bridging (LSB) models generally result in predictions that are specimen dependent. Hence, the measured behavior is not an intrinsic material property that is a true specimen-independent measure of toughness. In an effort to obtain such a measure for the MoSi$_2$/Nb composites, the weighted traction function (Equation 3) can be extrapolated to obtain an asymptotic value for specimens of

TABLE V Parameters used in the prediction for MoSi$_2$/Nb composite

Type of reinforcement	V_f	L (mm)	α	λ_b	ΔK_b (MPa$\sqrt{}$m)
200 μm Nb layer	0.2	3.5	1.4	2.7	11.5

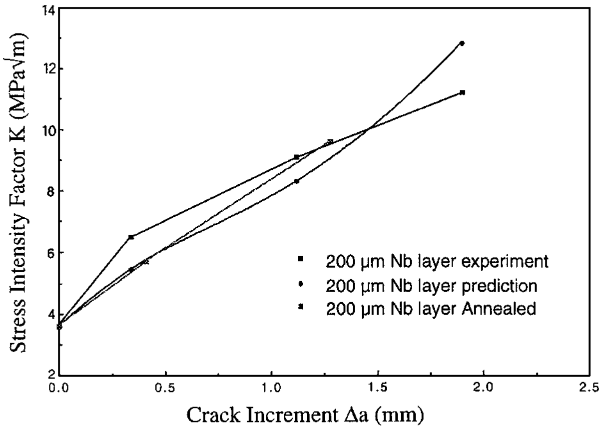

Figure 10 Effects of annealing on the resistance-curve behavior of $MoSi_2$/Nb composite.

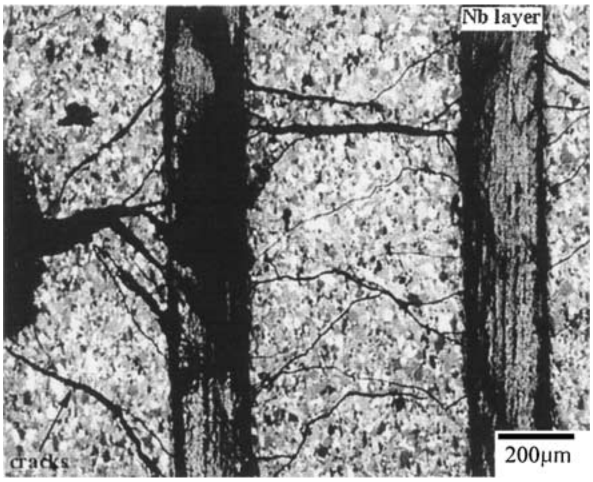

Figure 11 Crack/microstructure interactions and multiple matrix cracking in annealed in $MoSi_2$/Nb composite.

arbitrarily large width, W [18]. This results in predicted toughening levels that are true measures of intrinsic material toughness/steady-state toughness under small-scale bridging conditions. In the case of the $MoSi_2$/Nb composite, the asymptotic value of the intrinsic small-scale bridging steady-state toughness value is estimated to be 5.7 MPa$\sqrt{}$m.

It is of interest to examine the effects of annealing on the fracture behavior on the $MoSi_2$/Nb composite reinforced with 200 μm Nb Layer. The Layered $MoSi_2$/Nb composite was annealed in a vacuum furnace (10^{-6} Pa) at 1400°C for 24 hours to coarsen the interface. Single-Edge-Notched bend (SENB) specimens of the layered $MoSi_2$/Nb composite were also annealed at 1400°C for 24 hours under the same conditions. The effects of interfacial coarsening on fracture behavior was thus investigated by performing same resistance-curve experiments on the specimens. The resistance-curve obtained for the annealed layered composites is compared with the resistance-curve of the as-received one (Fig. 10). The annealed layer composite exhibits slightly lower initiation toughness and somewhat weaker resistance-curve (for Δa levels <1 mm) behavior than the as-received composite. This may be associated with lower interfacial strength after annealing.

Finally in this section, it is interesting to notice that multiple cracks were observed in the $MoSi_2$ matrix in all of the specimens (Fig. 11). Such multiple cracks may give rise to shielding/anti-shielding, depending on the spatial distributions and sizes of the cracks.

5.3. NiAl/V composites

In all NiAl/V composites, matrix crack initiation occurred in the NiAl at the matrix toughness level of ~6.6 MPa$\sqrt{}$m. However, the propagating cracks in the NiAl layers were retarded by the ductile vanadium layers. Subsequent crack growth, therefore, involved the re-initiation of cracks in the adjacent interfacial layers. Note that the cracks were bridged by the vanadium layers as they propagated through the NiAl/V composites. Also, although the vanadium layers were deformed plastically, none of them were observed to fracture during the development of large-scale bridging zones. Furthermore, fracture of the vanadium layers was only observed to occur at the onset of catastrophic failure.

A similar sequence of events was observed in all the composites (100, 200 and 400 μm layers) that were examined (Fig. 12 a–c). The crack/microstructure interactions illustrated in Fig. 12a and b are, therefore, comparable to those of all the other composites. It is also important to note here that propagating cracks stopped when they reached the vanadium layers (Fig. 12a). The measured resistance-curves therefore correspond to the interceptions of the propagating cracks with the ductile vanadium layers. Furthermore, a small plastic zone and some debonding were then observed in the vanadium, as the load was increased in an effort to re-initiate crack growth in the composites (Fig. 12a). Slip bands were observed to form along the ~45° orientation on both sides of the vanadium layers, as the load was increased further (Fig. 12b). Finally, stable crack growth was observed to re-nucleate from the slip bands into the adjacent interfacial layers.

In all cases, re-initiation occurred at a point that is offset somewhat from the initial mode I direction (Fig. 12b). This offset position, corresponding to an angle of ~45° to the initial mode I direction, is consistent with the positions of peak maximum shear strain that were computed in the detailed finite element simulation of the same NiAl/V composite systems [14].

Subsequent crack growth occurred along the deflected direction (~30° from the pure mode I direction), as shown in Fig. 12a and b, for composites reinforced with 100 and 200 μm thick vanadium layers. Unfortunately, however, re-nucleation in the case of the composites containing 400 μm thick layers (Fig. 4c) resulted in unstable crack growth and catastrophic failure. Also, the onset of unstable crack growth and catastrophic failure in the composites reinforced with 400 μm thick vanadium layers was associated with relatively high load increments (compared to those in the composites reinforced with 100 and 200 μm thick vanadium layers where re-nucleation of stable crack growth occurred in NiAl layers adjacent to the vanadium layers). The rates of change of crack driving force

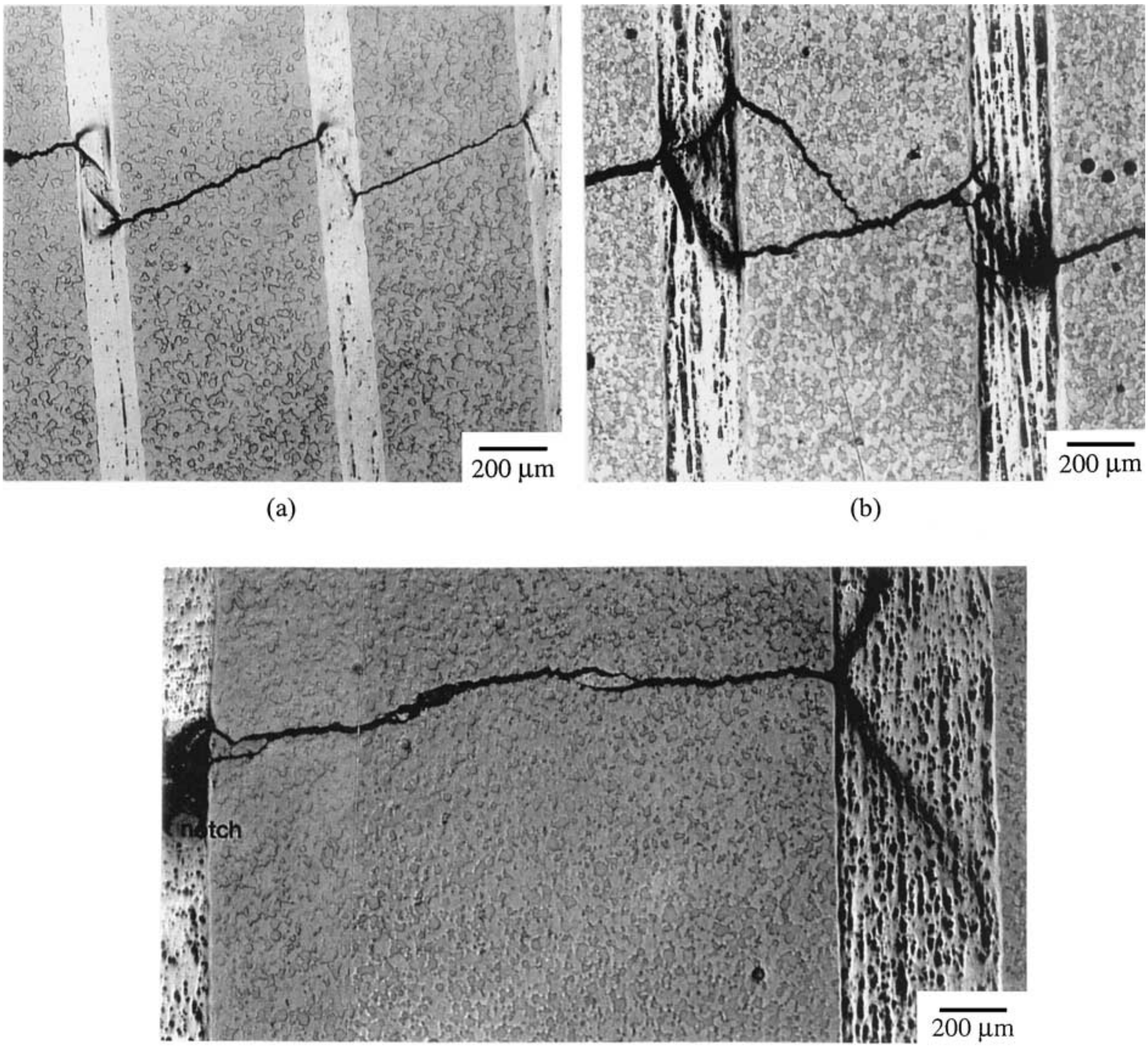

(a) (b)

(c)

Figure 12 Crack/microstructure interactions in NiAl/V composite (a) 100 μm V layers (b) 200 μm V layers (c) 400 μm V layers.

(with respect to crack length) were, therefore, close to the levels required for unstable crack growth upon renucleation of crack growth in the layers adjacent to the 400 μm thick vanadium layers.

The resistance-curves obtained from experiments for NiAl composites reinforced with 100 and 200 μm thick vanadium layers are shown in Fig. 13a and b, respectively. Each data point on the resistance curves

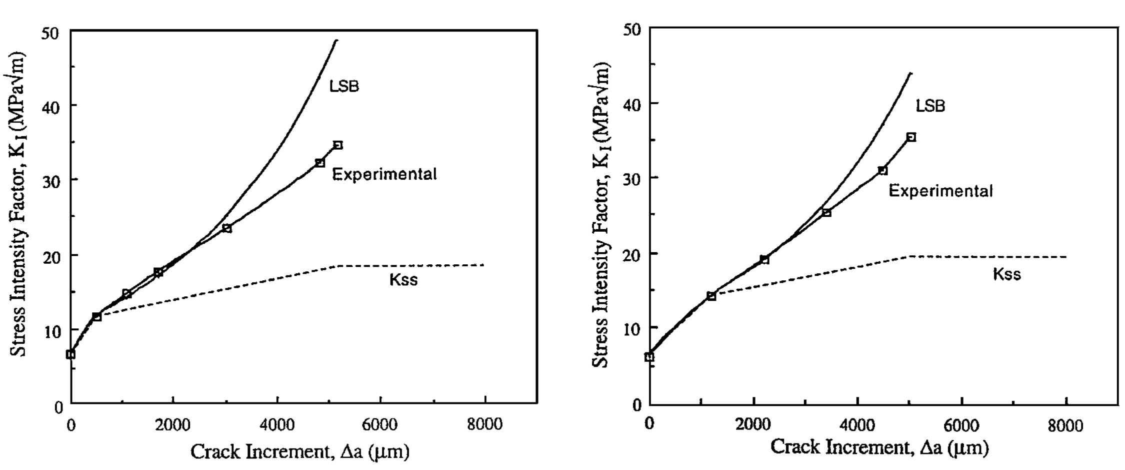

(a) (b)

Figure 13 Comparison of measured and predicted resistance-curves obtained for NiAl/V composites: (a) 100 μm V layers (b) 200 μm V layers.

TABLE VI Coefficients of fit polynomial used in the prediction for NiAl/V composite

	μ				
ν	0	1	2	3	4
0	0.4980	2.4463	0.0700	1.3187	−3.067
1	0.5416	−5.0806	24.3447	−32.7208	18.1214
2	−0.19277	2.55863	−12.6415	19.7630	−10.986

corresponds the position of a vanadium layer in front of the notch tip of the specimens. In both cases, resistance-curves increase significantly beyond the matrix toughness.

It is clear from the microscopic examination of the crack/layer interactions that crack-up shielding in NiAl/V composite occurred predominantly via crack bridging (Fig. 12). It is, therefore, of interest to examine the shielding effects due to crack bridging. The prediction of K_{lsb} employs the traction function, $\sigma(x)$, which depends on the stress-stretch relationships determined from the experiments on the single layer composite tensile tests. Here, $\sigma(x)$ is assumed as a constant and be equated to the yield stresses of the monolithic V foils.

The predicted large-scale bridging resistance-curves are presented in Fig. 13 using parameters summarized in Tables III and VI. Note that no large-scale bridging predictions were obtained for composites with 400 μm thick vanadium layers since bridging was not observed in these specimens. The large-scale bridging predictions are comparable to the measured resistance-curves. Similar large-scale bridging results have been reported in previous studies on other ductile phase toughened intermetallic matrices such as $\mathrm{MoSi_2}$/TZ-2Y/Nb [19], $\mathrm{Nb_3Al}$/Nb [4–6] and TiAl/TiNb [10].

Since neither the measured resistance-curves nor the large-scale bridging resistance-curves exhibit steady-state toughness values. An attempt has been made to obtain the specimen independent steady-state toughness, K_{ss}, from Equations 2–4 by assuming a specimen width that is significant greater than the length of bridge zone, i.e., simulating small-scale bridging conditions artificially. This approach, which was first applied by Bloyer *et al.* [5, 6] to $\mathrm{Nb_3Al}$/Nb layered composites, has the advantage of providing intrinsic toughness values that are essentially independent of specimen geometry differences. The calculated steady-state toughness values for NiAl/V composite are listed in Table VII. Note that the values of K_{ss} increase with increasing layer thickness (Table VII).

TABLE VII Calculated steady-state toughness values for NiAl/V composite

Layer thickness	Steady-state toughness K_{ss} (MPa$\sqrt{\mathrm{m}}$)
100 μm	18.4
200 μm	19.8

5.4. Implications

The current work shows that existing small- and large-scale bridging models provide adequate predictions of resistance-curve behavior in crack arrestor orientations of ductile layer toughened composites (Figs 6, 8 and 10). In all of the cases considered in this study, no fitting functions were needed to obtain good predictions in the small-scale and large-scale bridging regimes. The predictions were obtained simply by substitution of the independent measured material parameters into the appropriate equations for SSB and LSB.

The close agreement between the measured and predicted resistance-curves is very encouraging given the simplicity of the equations that were used for the predictions of SSB and LSB. Similar levels of predictive accuracy have been reported by Bloyer *et al.* [4–6] in their work on $\mathrm{Ni_3Al}$/Nb microlaminates. These studies show clearly that the simple bridging models are useful tools that are now sufficiently robust to guide the design of ductile phase toughened microlaminates.

More precise ductile bridging models by Zok and Hom [17], Odette *et al.* [10] and Cox [33, 34] require additional computational effort that may limited their

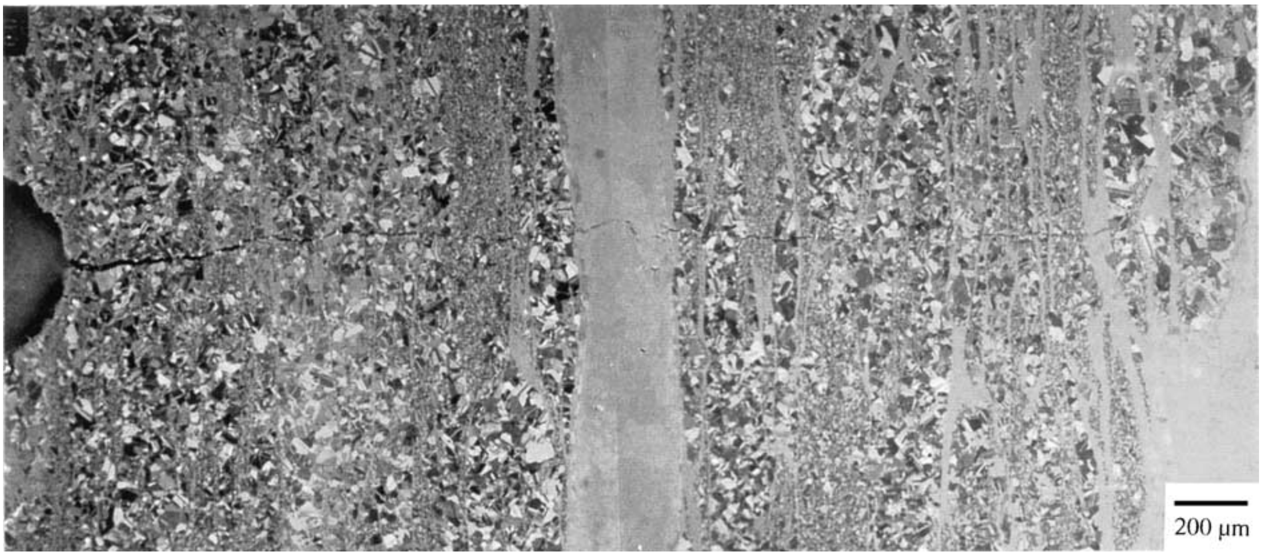

Figure 14 The interaction of fatigue crack path with microstructure in Ti-48Al/TiNb composite.

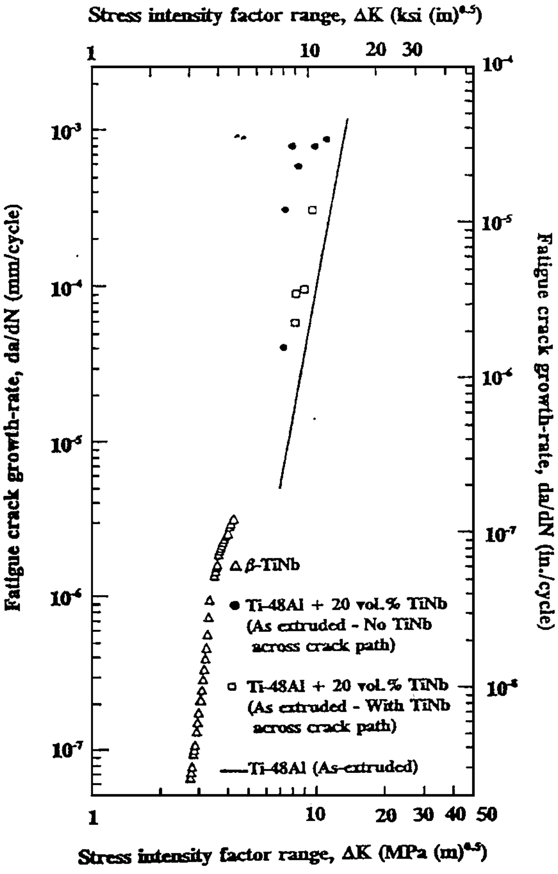

Figure 15 Fatigue crack growth data for Ti-48Al/TiNb composite.

use in the initial stages of composite design. However, such models are recommended in cases where the bridging tractions cannot be easily approximated by the weighted functions of Fett and Munz [29]. In such cases, the additional computational effort required by the use of more complex models is clearly justified.

Before closing, it is important to note that the improvements in ductile layer toughening obtained under monotonic loading may not necessarily apply under cyclic loading [3]. In the case of the Ti-48Al/TiNb composite, prior work by Soboyejo *et al.* [3] has shown that fatigue cracks extend into the TiNb strips, therby preventing the development of a significant bridging zone under cyclic loading (Fig. 14). In fact, fatigue crack growth in the Ti-48Al/TiNb composite occurred at faster rates compared to those in the Ti-48Al matrix (Fig. 15). Similar results have also been reported by Ritchie and co-workers [4–6] for other ductile phase toughened intermetallic systems. Hence, the measured improvements in resistance-curve behavior may not necessarily results in improvements in damage tolerance under cyclic loading.

However, in the case of the layered $MoSi_2$ intermetallics reinforced with Nb layers [3], recent results have shown that the layered reinforcement geometry results in improved fatigue crack growth resistance over that of Nb fiber-reinforced and Nb-particle reinforced composites. This is shown in Fig. 16, which is taken

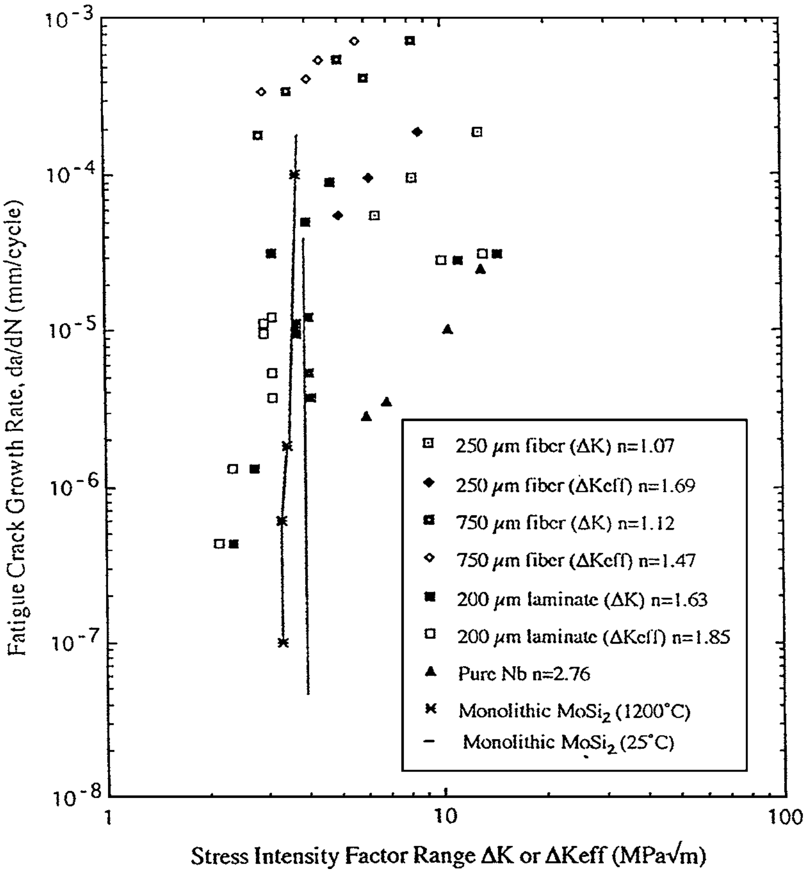

Figure 16 Fatigue crack growth data for $MoSi_2$/Nb composite.

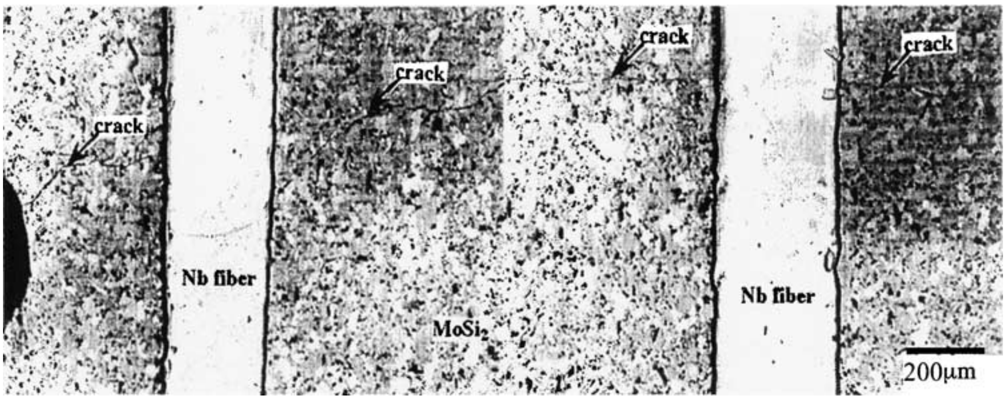

Figure 17 The interaction of fatigue crack path with microstructure in $MoSi_2$/Nb composite.

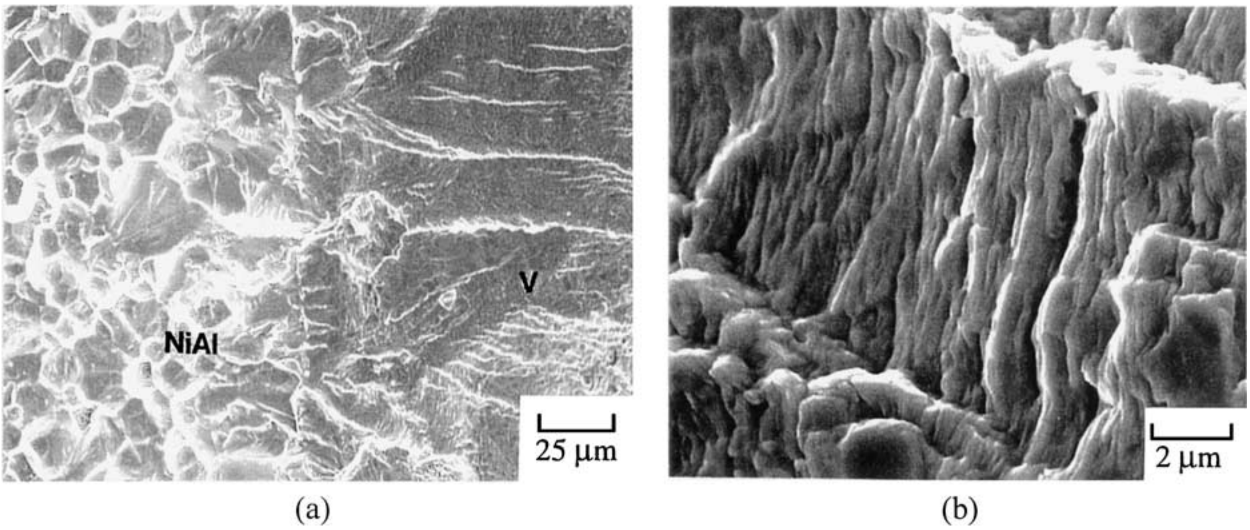

(a) (b)

Figure 18 Typical fatigue fracture modes in NiAl/V composite reinforced with 200 μm thick V layers: (a) cleavage in NiAl matrix and (b) ductile transgranular crack growth in V layer.

from [3]. The improved fatigue crack growth resistance in the Nb layer-reinforced composite is associated with the shielding effects of crack bridging by the Nb layers (Fig. 17). Also, the poorer fatigue resistance of the Nb fiber-reinforced $MoSi_2$ composites is due to the degradation of the bridging zones due to fiber cracking under cyclic loading [3]. The Nb particulates did not bridge the cracks, and hence the poorest fatigue crack growth resistance in the $MoSi_2$/Nb particulate system is associated with the absence of crack bridging, and the limited shielding contributions from continuous crack deflection by tilting and twisting around Nb particulate reinforcements [3].

Finally in this section, it is important to note that the NiAl/V microlaminates have also been shown to exhibit some resistance to fatigue crack growth. Although very limited data is available, the faster crack growth rates in the NiAl layers are associated with a cyclic cleavage fracture mode (Fig. 18a), while the slower crack growth rates in the V layers are associated with a ductile transgranular fracture mode (Fig. 18b). The presence of ductile layer reinforcements, therefore, appear to promote stable crack growth in ductile phase toughened brittle matrix composites. However, the fatigue crack growth rates in the brittle phases are still too fast to make these systems serious contenders for structural applications in high temperature systems.

6. Conclusions

The resistance-curve behavior of ductile layer toughened intermetallics has been studied within a combined experimental and theoretical framework. The following conclusions have been reached from a study of Ti-48Al/TiNb, $MoSi_2$/Nb and NiAl/V composites:

1. Ductile phase toughening occurs primarily via small- and large-scale bridging mechanisms in the crack-arrestor orientation. These give rise to strong resistance curve behavior during the early stages of stable crack growth, and a gradual evolution towards a steady-state in the large-scale bridging regime.
2. The measured and predicted resistance curves are generally in good agreement in the small- and large-scale bridging regimes. In general, the small-scale bridging model provides good estimates of ductile layer bridging for crack extension levels, Δa, below ~0.6 mm. The SSB model also predicts the curvature of the measured resistance curves in this regime. In contrast, the LSB does not predict the measured curvatures of the resistance-curves, although it does predict the magnitudes of the measured resistance curves.
3. The measured and predicted resistance curves presented in this paper are specimen-dependent. Hence, they are not intrinsic material properties or measures

of intrinsic toughness. However, estimates of intrinsic toughness can be obtained by a weight function extrapolation method for many ductile phase toughened intermetallic matrices. This predicts intrinsic toughness values of: 5.7 MPa$\sqrt{m}$ for the $MoSi_2$/Nb microlaminate, and 18.4–19.4 MPa$\sqrt{m}$ for the NiAl/V microlaminate. The latter appear to increase with increasing V layer thickness.

Acknowledgements

This research was completed with the support of grants from the National Science Foundation (Grant No. CMS-9634870 and Grant No. DMR-9458018) and the Office of Naval Research (Grant No. N-00014-94-1-0501). Appreciation is extended to the NSF Program Monitors (Dr. Bruce MacDonald and Dr. Dan Davis) and the ONR Program Monitor (Dr. George Yoder) for their encouragement and support.

References

1. V. D. KRSTIC, P. S. NICHOLSON and R. G. HOAGLAND, *J. Amer. Ceram. Soc.* **64** (1981) 499.
2. V. D. KRISTIC, *Phil. Mag.* **48** (1983) 695.
3. W. O. SOBOYEJO, F. YE, L.-C. CHEN, N. BAHTISH, D. S. SCHWARTZ and R. J. LEDERICH, *Acta Mater.* **44** (1996) 2027.
4. D. R. BLOYER, K. T. VENKATESWARA RAO and R. O. RITCHIE, *Mater. Sci. Eng.* A **A216** (1996) 80.
5. *Idem.*, *Metall. Mater. Trans.* A **29A** (1998) 2483.
6. *Idem.*, *ibid.* **30A** (1999) 633.
7. M. Y. HE, F. E. HEREDIA, D. J. WISSUCHEK, M. C. SHAW and A. G. EVANS, *Acta Metall. Mater.* **41** (1993) 1223.
8. X. F. CHEN, D. R. JOHNSON, R. D. NOEBE and B. F. OLIVER, *J. Mater. Res.* **10** (1995) 1159.
9. S. M. JOSLIN, X. F. CHEN, B. F. OLIVER and R. D. NOEBE, *Mater. Sci. Eng.* A **A196** (1995) 9.
10. G. R. ODETTE, B. L. CHAO, J. W. SHECKHERD and G. E. LUCAS, *Acta Metall. Mater.* **40** (1992) 2381.
11. P. R. SUBRAMANIAN, M. G. MENDIRATTA and D. B. MIRACLE, *Metall. Mater. Trans.* A **25A** (1994) 2769.
12. J. KAJUCH, J. SHORT and J. J. LEWANDOWSKI, *Acta Metall. Mater.* **43** (1995) 1955.
13. L. SHAW and R. ABBASCHIAN, *ibid.* **42** (1994) 213.
14. M. LI, R. WANG, N. KATSUBE and W. O. SOBOYEJO, *Scripta Mater.* **40** (1999) 397.
15. M. F. ASHBY, F. J. BLUNT and M. BANNISTER, *Acta Metall.* **37** (1989) 1847.
16. B. BUDIANSKY, J. C. AMAZIGO and A. G. EVANS, *J. Mech. Phys. Solids* **36** (1988) 167.
17. F. ZOK and C. L. HOM, *Acta Metall. Mater.* **38** (1990) 1895.
18. M. LI and W. O. SOBOYEJO, *Metall. Mater. Trans.* A **31A** (2000) 1385.
19. H. C. CAO, B. J. DALGLEISH, H. E. DEVE, C. ELLIOTT, A. G. EVANS, R. MEHRABIAN and G. R. ODETTE, *Acta. Metall.* **37** (1989) 2969.
20. H. E. DEVE and M. J. MALONEY, *Acta Metall. Mater.* **39** (1991) 2275.
21. M. BANNISTER, H. SHERCLIFF, G. BAO, F. ZOK and M. F. ASHBY, *ibid.* **40** (1992) 1531.
22. F. E. HEREDIA, M. Y. HE, G. E. LUCAS, A. G. EVANS, H. E. DEVE and D. KONITZER, *ibid.* **41** (1993) 505.
23. W. O. SOBOYEJO, K. T. VENKATESWARA RAO, S. M. L. SASTRY and R. O. RITCHIE, *Metall. Trans.* A **24A** (1993) 585.
24. P. RAMASUNDARAM, R. BOWMAN and W. O. SOBOYEJO, *Mater. Sci. Eng.* A **A248** (1998) 132.
25. P. A. MATAGA, *Acta Metall.* **37** (1989) 3349.
26. W. J. CLEGG, *Acta. Metall. Mater.* **40**(11) (1992) 3085.
27. W. J. CLEGG and L. R. SEDDON, in 2nd European Conference on Advanced Materials, Euromat ‘91, edited by T. W. Clyne and P. J. Withers (Institute of Materials, Cambridge, UK, 1992) Vol. 2, p. 266.
28. F. YE, M. LI and W. O. SOBOYEJO, *J. Amer. Ceram. Soc.* **42** (1999) 2460.
29. T. FETT and D. MUNZ, “Stress Intensity Factors and Weight Functions for One-Dimensional Cracks” (Institut fur Materialforschung, Kernforschungszentrum, Karlsryhe, Germany, 1994).
30. H. TADA, P. C. PARIS and G. R. IRWIN, “The Stress Analysis of Cracks Handbook” (Del Research, St. Louis, MO, 1985).
31. L. R. F. ROSE, *J. Mech. Phys. Solids* **35** (1987) 383.
32. K. L. JOHNSON, “Contact Mechaniscs” (Cambridge University Press, Cambridge, UK, 1985).
33. B. N. COX and C. S. LO, *Acta Metall. Mater.* **40** (1992) 69.
34. B. N. COX and L. R. F. ROSE, *Mech. Mater.* **22** (1996) 249.
35. T. C. LU, A. G. EVANS, R. J. HECHT and R. MEHRABIAN, *Acta Metall. Mater.* **39** (1991) 1853.
36. S. SURESH and J. R. BROCKENBROUGH, *Acta Metall.* **36** (1988) 1444.
37. F. YE, Ph.D thesis, 1997.

Received 22 March
and accepted 21 November 2001